

Probing Neutrinos from Planck and Forthcoming Galaxy Redshift Surveys

Yoshitaka Takeuchi and Kenji Kadota

Department of Physics, Nagoya University, Nagoya 464-8602, Japan

E-mail: yoshitaka@nagoya-u.jp, kadota.kenji@f.nagoya-u.jp

Abstract.

We investigate how much the constraints on the neutrino properties can be improved by combining the CMB, the photometric and spectroscopic galaxy redshift surveys which include the CMB lensing, galaxy lensing tomography, galaxy clustering and redshift space distortion observables. We pay a particular attention to the constraint on the neutrino mass in view of the forthcoming redshift surveys such as the Euclid satellite and the LSST survey along with the Planck CMB lensing measurements. Combining the transverse mode information from the angular power spectrum and the longitudinal mode information from the spectroscopic survey with the redshift space distortion measurements can determine the total neutrino mass with the projected error of $\mathcal{O}(0.02)\text{eV}$. Our analysis fixes the mass splittings among the neutrino species to be consistent with the neutrino oscillation data, and we accordingly study the sensitivity of our parameter estimations on the minimal neutrino mass. The cosmological measurement of the total neutrino mass can distinguish between the normal and inverted mass hierarchy scenarios if the minimal neutrino mass $\lesssim 0.005\text{ eV}$ with the predicted $1\text{-}\sigma$ uncertainties taken into account.

Keywords: neutrino masses from cosmology, cosmological parameters from CMBR, redshift surveys, gravitational lensing

Contents

1	Introduction	1
2	The massive neutrinos in cosmology	3
3	Cosmological observables	4
3.1	Angular power spectrum	4
3.1.1	The redshift distribution of source galaxies	6
3.2	Three-dimensional galaxy power spectrum	7
4	Fisher matrix formalism	8
4.1	The Fisher matrix for the angular power spectrum	9
4.2	The Fisher matrix for the three-dimensional galaxy power spectrum	12
5	Results	14
6	Discussion and conclusion	20

1 Introduction

There has been an ever-growing evidence supporting the non-vanishing neutrino masses from the measurements of the neutrino oscillations [1, 2] including the solar (ν_e), atmospheric ($\nu_\mu, \bar{\nu}_\mu$), reactor ($\bar{\nu}_e$) and accelerator (ν_μ) neutrino experiments [3]. There also have been the precise measurements of the cosmological observables such as the cosmic microwave background (CMB) which favor the non-vanishing neutrino masses [4, 5].

We in this paper forecast the strong constraints on the neutrino masses from the observations of the large-scale structure (LSS) and CMB. The different astrophysical probes on the neutrino masses are of great interest for their complementarity and for their reducing the degeneracies among the relevant parameters. The current cosmological data have put the upper bounds of order $\sum m_\nu \lesssim 0.2\text{-}0.5$ eV and there also have been numerous theoretical studies for the future forecasts on the neutrino mass constraints claiming even an order of magnitude improvements from the cosmological measurements such as the CMB, galaxy weak lensing, galaxy clustering, galaxy cluster count, baryon acoustic oscillations, Type Ia supernovae and Lyman- α forest [6–35]. For the CMB and LSS observables, for instance, the unprecedented precision on the neutrino mass constraints can be expected from the on-going and forthcoming experiments such as the Planck [36], SPTPol [37], ACTPol [38] providing the CMB lensing measurements, and a number of wide-field surveys for both ground-based imaging surveys and space-based missions such as the Subaru Hyper Suprime-Cam Survey (HSC¹)

¹<http://www.naoj.org/Projects/HSC/index.html>

[39], the Dark Energy Survey (DES²) [40], the Large Synoptic Sky Survey (LSST³) [41], and the European Space Agency (ESA) Euclid satellite mission⁴ [42].

To realize the tighter constraints on the neutrinos, however, we need to break the degeneracies among the cosmological parameters, e.g. the degeneracies among the neutrino mass and the dark energy parameters. One of the sound tactics to lift the degeneracies is to combine multiple observables and to take the cross-correlations among those observables which have the different dependence on the cosmological parameters of our interest. Our study therefore emphasizes the merit of combining the angular power spectrum, in particular the CMB lensing and photometric galaxy lensing tomography, and the three-dimensional galaxy power spectrum from the spectroscopic redshift survey which possesses not only the transverse mode information but also the information along the line of sight. We, for this purpose, perform a Fisher matrix analysis by combining the angular power spectrum and the three-dimensional galaxy power spectrum, and we investigate how accurately the property of the neutrino can be constrained from the on-going and upcoming surveys. We, for concreteness, adopt the Planck, LSST and Euclid surveys as the reference surveys in the following, deferring to the discussion section the quantitative comparison with the analogous analysis using the on-going experiments HSC and DES instead of the future experiment LSST.

We also seek the distinction between two neutrino mass structures, normal $m_{\nu_1} < m_{\nu_2} \ll m_{\nu_3}$ and inverted $m_{\nu_3} \ll m_{\nu_1} < m_{\nu_2}$ mass hierarchy scenarios which are the fiducial models in our forecasts. For the fiducial values of the neutrino mass splittings, we take the best fit values for the atmospheric neutrino $|\Delta m_{31(32)}^2|$ (the parenthesis is for the inverted hierarchy) and the solar neutrino parameter Δm_{21}^2 based on the global analysis of neutrino oscillation data including the recent measurements of the neutrino mixing angle θ_{13} at the reactor experiments [43]

$$|\Delta m_{31(32)}^2| = 2.47(2.46) \times 10^{-3} \text{ eV}^2, \quad \Delta m_{21}^2 = 7.54 \times 10^{-5} \text{ eV}^2, \quad (1.1)$$

where $\Delta m_{ij} \equiv m_{\nu_i}^2 - m_{\nu_j}^2$. The minimal neutrino mass $m_{\nu,\text{min}}$, which corresponds to $m_{\nu_1}(m_{\nu_3})$ for the normal (inverted) mass spectrum, is undetermined from the oscillation data, and we also study the sensitivity of the neutrino parameter estimation on the value of $m_{\nu,\text{min}}$.

This paper is organized as follows. We first briefly review the effects of the massive neutrinos on the cosmological observables in Section 2. In Section 3, we summarize the cosmological observables used in the analysis and how those observables are theoretically treated in terms of the angular power spectrum and the three-dimensional galaxy power spectrum. Section 4 describes our Fisher matrix analysis and Section 5 presents the main results on the improvement in the neutrino property constraints by combining the CMB, the photometric redshift survey and the spectroscopic redshift survey. Section 6 is devoted to the discussion and conclusion.

²<http://darkenergysurvey.org>

³<http://www.lsst.org>

⁴<http://www.euclid-ec.org>

2 The massive neutrinos in cosmology

We start with a brief review on the effects of the neutrinos on the CMB and structure formation. Because a neutrino becomes non-relativistic around $1 + z \sim 300$ ($m_\nu/0.05$ eV) when the temperature becomes comparable to its mass, we assume, unless stated otherwise, the sub eV mass neutrinos of our interest become non-relativistic during the matter domination era.

The massive neutrinos lighter than a half eV are relativistic at the recombination epoch and their effects of reducing the matter-radiation ratio on the CMB are manifest in the early integrated Sachs-Wolfe (ISW) effect. The massive neutrinos deep in the matter domination epoch and in the dark energy domination epoch can also cause the decay of the gravitational potential enhancing the late ISW effect [6, 8, 44–46]. Those effects imprinted in the primary CMB anisotropy can however be also induced by varying other cosmological quantities such as the Hubble parameter and the equation of state parameter w [47–49]. The CMB lensing turns out to be quite powerful in breaking the parameter degeneracies which would otherwise be persistent in the CMB power spectrum because the lensing is sensitive not only to the geometry but also to the growth of the structure along the line of sight, and the recent impressive progress on the CMB lensing measurements would be of great interest for the exploration of the neutrino properties. The CMB lensing reconstruction from the temperature anisotropies alone has the limitation due to its statistical noise and it benefits significantly from the polarization measurements probing the smaller scales with high precision [50].

The matter power spectrum can be affected by the neutrinos because the structure formation is suppressed due to the free-streaming of the neutrinos for the scales below the neutrino Jeans length scale [51]. The neutrino comoving free-streaming scale decreases as $\lambda_{\text{FS}} \propto a^{-1/2}$ during the matter domination so that the turn-over scale of the matter power spectrum due to the neutrino suppression has the upper bound corresponding to the neutrino free-streaming scale when it becomes non-relativistic. Each different mass neutrino has a different free-streaming scale and hence the matter power spectrum in principle can probe each neutrino mass rather than just a sum of neutrino masses. For instance, even if the value for a total neutrino mass is identical, the error on the total neutrino mass from a galaxy redshift survey can differ depending on the neutrino mass splitting patterns [11, 24, 52]. The neutrino free-streaming scale during the matter domination is

$$k_{\text{FS}} \sim 0.015 \text{Mpc}^{-1} \left(\frac{m_\nu}{0.05 \text{eV}} \right) \sqrt{\frac{\Omega_m h^2}{0.14} \frac{1}{1+z}} \quad (2.1)$$

This suppression turn-over scale is proportional to the neutrino mass, hence the finding this suppression scale can probe each neutrino mass scale while the overall amplitude suppression gives us the information on the sum of the neutrino masses. Too light a neutrino becomes hard to be probed by the galaxy survey because k_{FS} may become too small for the survey volume to cover, even though other measurements such as the CMB observables can compliment such deficiencies. The free-streaming scale is also dependent on the redshift, and the spectroscopic galaxy redshift survey with the

accurate redshift information would be of great help to probe the neutrino features imprinted in the matter fluctuations. For $k < k_{\text{FS}}$, the non-relativistic neutrinos falls into the gravitational potential along with the cold dark matter (CDM) and baryons, and the conventional picture for the matter fluctuation growth proportional to the standard linear growth factor $D(z)$ applies. For $k > k_{\text{FS}}$ with the neutrino free-streaming effects operative, the non-relativistic neutrinos cannot cluster because of too large a velocity dispersion. The growth of the matter fluctuations hence is slower compared with that for $k < k_{\text{FS}}$, and the suppressed power is proportional to $(1 - f_\nu)D(z)^{1-p}$ for $k \gg k_{\text{FS}}$ with $p = (5 - \sqrt{25 - 24f_\nu})/4$ and $f_\nu \equiv \Omega_\nu/\Omega_m$ [44, 51, 53, 54]. Hence, for a scale below the current free-streaming scale, the matter power spectrum is suppressed roughly by a fraction $\Delta P_m(k)/P_m(k) \sim -8f_\nu$ with an even bigger suppression in the non-linear regime [55, 56]). Due to the dependence of the matter power on $f_\nu \propto \sum m_\nu/\Omega_m h^2$, the neutrino mass is also degenerate with $\Omega_m h^2$ [56] even though the precise measurement of Ω_m from other experiments such as the Planck makes m_ν - $\Omega_m h^2$ degeneracy less significant. We also benefit from combing the linear scale galaxy redshift survey and the galaxy lensing survey because the lensing is disadvantageous for being sensitive to the mass clustering at the non-linear scales. A potential problem in probing the galaxy clustering is the issue of the bias which hinders the direct probe on the matter clustering and hence leads to the uncertainties in the neutrino mass constraints. Combing the spectroscopic redshift survey data and the galaxy weak lensing tomography data can help reduce the bias uncertainty and hence can improve the neutrino mass constraints as we shall discuss in the following.

3 Cosmological observables

We here summarize the cosmological observables used in our analysis. In this work, we investigate the constraints from the data combining three kinds of cosmological surveys: the CMB experiment, the photometric redshift survey and the spectroscopic redshift survey. The observables from the CMB experiment and the photometric redshift survey are the projected two-dimensional data, providing the angular power spectra C_ℓ . The spectroscopic redshift survey can give us the three-dimensional power spectrum $P(\mathbf{k})$ providing the information for not only the transverse direction but also for the line-of-sight direction.

3.1 Angular power spectrum

The angular power spectrum for auto- and cross-correlations of the observables X and Y can be given by

$$C_\ell^{XY} = \frac{2}{\pi} \int k^2 dk P_m(k) \Delta_\ell^X(k) \Delta_\ell^Y(k), \quad (3.1)$$

where $P_m(k)$ is the matter power spectrum at present and Δ_ℓ^X is the kernel of the observable X . We consider the CMB temperature anisotropies (T), E -mode polarization (E), CMB lensing potential (ψ), the galaxy distributions (g_i) and the galaxy weak

lensing shear (γ_i), i.e. $X \in \{T, E, \psi, g_i, \gamma_i\}$, as the observables for the angular power spectra. The observables T and E are the unlensed ones, and the information of the CMB lensing is included just in the CMB lensing potential ψ . The subscript on the galaxy distributions and the weak lensing shear represents the i -th redshift bin in the tomographic surveys.

The temperature and E -mode polarization angular power spectra are obtained from a publicly available code CAMB [57]. The cross-correlation for Tg_i and that for $T\gamma_i$ arise from the late ISW effect [58] and the kernel of the late ISW is given by

$$\Delta_\ell^{\text{ISW}}(k) = 3\Omega_{\text{m},0}H_0^2 \int_0^{z_*} dz \frac{d}{dz} [D(z, k)(1+z)] \frac{j_\ell(kr(z))}{k^2}, \quad (3.2)$$

where z_* represents the redshift of the last scattering surface, $r(z)$ is the comoving distance to the redshift z , $\Omega_{\text{m},0}$ and H_0 are respectively the matter density parameter and the Hubble parameter at the present time. The function $D(z, k) \equiv \sqrt{P_{\text{m}}(k, z)/P_{\text{m}}(k, 0)}$ represents the growth factor, $P_{\text{m}}(k, z)$ represents the matter power spectrum at redshift z and $j_\ell(kr(z))$ is the spherical Bessel function.

The CMB photons coming from the last scattering surface are deflected by the potential gradients of the LSS along the line-of-sight [59], hence the CMB lensing potential also has the correlation with the LSS. For the CMB lensing potential, the kernel is give by

$$\Delta_\ell^\psi(k) = 3\Omega_{\text{m},0}H_0^2 \int_0^{r_*} dr \frac{r_* - r}{rr_*} \frac{D(z(r), k)}{a(r)} \frac{j_\ell(kr)}{k^2}, \quad (3.3)$$

where r_* represents the comoving distance to the last scattering surface.

We can obtain two kinds of observables from the photometric redshift survey; one is the distribution of galaxies and the other is the galaxy weak lensing. For the galaxy distributions, we consider the tomographic survey with some redshift bins, and the kernel of the galaxy distributions is given by

$$\Delta_\ell^{g_i}(k) = \int_{z_i}^{z_{i+1}} dz b(z) \frac{n_i(z)}{n_i^{\text{A}}} D(z, k) j_\ell(kr(z)), \quad (3.4)$$

where $b(z)$ is the biasing parameter of galaxy and $n(z)$ and n_i^{A} represent the redshift distribution of sample galaxies and its normalization factor respectively. We adopt a time-varying linear biasing parameter by the first-order expansion $b(z) = b_0 + b_1 z$. We treat these two model parameters b_0 and b_1 as free parameters in our analysis and the fiducial values are set to $(b_0, b_1) = (1.0, 0.8)$ [60].

We also assume the tomographic survey for the galaxy weak lensing. The galaxy weak lensing survey measure the shear of source galaxies due to the distributions of foreground galaxies. For the galaxy weak lensing shear, the kernel is given by

$$\Delta_\ell^{\gamma_i}(k) = \int_0^\infty dr W_{\ell,i}(r(z)) D(z(r), k) \frac{j_\ell(kr(z))}{k^2}, \quad (3.5)$$

with

$$W_{\ell,i}(r(z)) = \frac{3\Omega_{m,0}H_0^2}{2ar(z)} \sqrt{\frac{(\ell+2)!}{(\ell-2)!}} \int_{\max(z,z_i)}^{z_{i+1}} dz_s \frac{n(z_s)}{n_i^A} \frac{r(z_s) - r(z)}{r(z_s)}. \quad (3.6)$$

The weak lensing tomography provides us with a projected density estimator for each redshift bin of the source galaxies, and hence possesses the significant cross-correlations with the galaxy distribution observables.

3.1.1 The redshift distribution of source galaxies

We here assume the redshift distribution of sample galaxies is give by the following analytic form [61, 62];

$$N(z) \propto z^\alpha \exp \left[- \left(\frac{z}{z_0} \right)^\beta \right], \quad (3.7)$$

where $N(z)$ should be normalized as $\int N(z)dz = 1$, and we can then rewrite the redshift distribution function of sample galaxies as,

$$N(z) = \frac{n(z)}{\bar{n}_g} = \frac{\beta}{\Gamma[(\alpha+1)/\beta]} \frac{z^\alpha}{z_0^{\alpha+1}} \exp \left[- \left(\frac{z}{z_0} \right)^\beta \right]. \quad (3.8)$$

We adopt $\alpha = 2.0$, $\beta = 1.5$, and z_0 is determined from the relation with mean redshift z_m defined as

$$z_m = \int z \frac{n(z)}{\bar{n}_g} dz = z_0 \frac{\Gamma[(\alpha+2)/\beta]}{\Gamma[(\alpha+1)/\beta]}. \quad (3.9)$$

The normalization of the redshift distribution function is fixed by the total number density of sample galaxies and defined as,

$$n^A \equiv \int_0^\infty dz n(z). \quad (3.10)$$

We next consider the tomographic surveys, which divide the sample galaxies into some redshift bins, and analytically include the effect of photometric redshift errors following the model of [63] as

$$p_i(z_{\text{ph}}|z) = \frac{1}{\sqrt{2\pi}\sigma_z(z)} \exp \left[- \frac{(z - z_{\text{ph}})^2}{2\sigma_z^2(z)} \right], \quad (3.11)$$

where $\sigma_z(z)$ denotes the redshift scatter systematics and we assume the following redshift dependence:

$$\sigma_z(z) = \sigma_z^{(i)}(1+z), \quad (3.12)$$

In this paper we assume only the redshift scatter systematics with $\sigma_z^{(i)} = 0.03$ for each redshift bin. We can then write the redshift distribution of sample galaxies in the i -th redshift bin with the effect of photometric redshift errors as

$$n_i(z) = \int_{z_{\text{ph}}^{(i)}}^{z_{\text{ph}}^{(i+1)}} dz_{\text{ph}} N(z) p_i(z_{\text{ph}}|z) = \frac{1}{2} [\text{erf}(x_{i+1}) - \text{erf}(x_i)] n(z), \quad (3.13)$$

with $x_i \equiv (z_{\text{ph}}^{(i)} - z)/\sqrt{2}\sigma_z(z)$ and the redshift distribution of galaxy samples $n(z)$ defined in Eq. (3.8). In the same manner with Eq. (3.10), the total number density of sample galaxies in the i -th redshift bin can be given as,

$$n_i^{\text{A}} \equiv \int_0^\infty dz n_i(z). \quad (3.14)$$

In the following analysis, we assume a fixed number of photometric redshift bins ($N^{\text{ph}} = 5$), and we determine the ranges of redshift for each redshift bin keeping the same number of sample galaxies for each bin. To see the dependence of the binning scheme on our parameter estimation, we compare the parameter constraints with different numbers of redshift bins in the discussion section Sec. 6.

3.2 Three-dimensional galaxy power spectrum

In analyzing the three-dimensional redshift space galaxy power spectrum, we restrict our discussions to the linear scale unless stated otherwise. The galaxy over-density δ_{g} is distorted along the line of sight due to the coherent infall bulk motion of galaxies, and it has, in the plane parallel approximation (the galaxies are far away from the observers so that the displacement due to the peculiar velocities are parallel to each other), a simple form in the Fourier space [64],

$$\delta_{\text{g}}(k, \mu) = b(z) [1 + \beta(z, k)\mu^2] \delta(k, z), \quad (3.15)$$

where $b(z)$ is the scale-independent linear bias parameter and β is the redshift space distortion parameter defined as

$$\beta(z, k) = \frac{1}{b(z)} \frac{\partial \ln D(z, k)}{\partial \ln a}. \quad (3.16)$$

The magnitude of the wave number is $k = \sqrt{k_\perp^2 + k_\parallel^2}$, where k_\perp and k_\parallel are the wave numbers across and along the line of sight, and μ represents the cosine of the angle θ between the line of sight and the wave vector, $\mu^2 \equiv \cos^2 \theta = k_\parallel^2/(k_\parallel^2 + k_\perp^2)$.

In addition, the wrong assumption of the reference cosmological model also produces the distortion in the measured power spectrum, known as the geometrical distortion [65–67]. What we need in the measurements of three-dimensional galaxy power spectrum is the positions in the 3-dimensional space, though we measure the angular positions of galaxies on the sky and the radial positions of galaxies in the redshift space. We therefore need assume a reference cosmological model for the mapping of the observed angular and redshift positions to the one in the 3-dimensional space. We take the reference cosmology to be the fiducial cosmology for simplicity in the following.

The comoving size of an object in the radial r_\parallel and transverse r_\perp directions, which extends $\Delta\theta$ in the angle and Δz in the redshift, is estimated as

$$r_\parallel = \frac{\Delta z}{H(z)}, \quad \text{and} \quad r_\perp = D_{\text{A}}(z)\Delta\theta, \quad (3.17)$$

where we need to assume some cosmological model for the estimation of $H(z)$ and the angular diameter distance $D_A(z)$. Then the relations between the fiducial wave numbers and the true wave numbers are estimated from the inverse of r_{\parallel} and r_{\perp}

$$k_{\parallel} = \frac{H(z)}{H^{(\text{fid})}(z)} k_{\parallel}^{(\text{fid})}, \quad \text{and} \quad k_{\perp} = \frac{D_A^{(\text{fid})}(z)}{D_A(z)} k_{\perp}^{(\text{fid})}, \quad (3.18)$$

where we distinguish the quantities in the fiducial cosmological model by the subscript “fid”. Then the galaxy power spectrum estimated in redshift space is modeled as [68]

$$P_g(k_{\parallel}^{(\text{fid})}, k_{\perp}^{(\text{fid})}, z) = \frac{D_A^{(\text{fid})}(z)^2 H(z)}{D_A(z)^2 H^{(\text{fid})}(z)} b(z)^2 [1 + \beta(z, k)\mu^2]^2 P_m(k, z), \quad (3.19)$$

where the factor $D_A^{(\text{fid})}(z)^2 H(z)/D_A(z)^2 H^{(\text{fid})}(z)$ represents the geometrical distortion [65]. We can see from Eq. (3.19) that using the galaxy power spectrum for the cosmological parameter estimation would suffer from the degeneracies among the biasing parameter $b(z)$, the redshift distortion parameter $\beta(z, k)$ and the growth factor of the matter density fluctuations $D(z, k)$. As we shall discuss in the following sections, these degeneracies can be lifted by taking the cross correlations with other measurements.

We use the publicly available Boltzmann code CAMB [57] to get the transfer functions of the CMB observables and matter power spectrum with massive neutrinos and calculate the corresponding all auto- and cross-correlations.

4 Fisher matrix formalism

For forecasting the cosmological parameter estimations, we calculate the Fisher matrix (FM) which represents the curvature of the likelihood function around its maximum in a given parameter space defined as

$$F_{\alpha\beta} \equiv \left\langle -\frac{\partial^2 \ln L}{\partial p_{\alpha} \partial p_{\beta}} \right\rangle \quad (4.1)$$

where L is the likelihood function for the data set of our interest given the theoretical model parameters $\mathbf{p} = \{p_1, p_2, \dots\}$ and the sub-scripts α and β run over the model parameters. The FM formalism tells us how accurately the given observation can measure the cosmological parameters around the fiducial model, and the marginalized one-sigma error bound for a parameter p_{α} is given by $\sigma(p_{\alpha}) = \sqrt{(\mathbf{F}^{-1})_{\alpha\alpha}}$ from the Cramer-Rao inequality.

As for our our fiducial cosmological model, we assume the flat Λ CDM plus massive neutrino model in our analysis and we include the following 13 cosmological parameters;

$$\mathbf{p} \in \{100\Omega_b h^2, \Omega_c h^2, \Omega_{\Lambda}, f_{\nu}, \tau, Y_p, n_s, A_s, \alpha_s, w, N_{\text{eff}}, b_0, b_1\}. \quad (4.2)$$

Ω_b , Ω_c and Ω_{Λ} are respectively the density parameters of the baryon, CDM and the cosmological constant Λ . $h \equiv H_0/100$ represents the Hubble parameter. f_{ν} is the

fraction of the massive neutrinos in the matter component, defined as $f_\nu \equiv \Omega_\nu/\Omega_m$ and Ω_ν is the density parameter of the massive neutrino. τ is the optical-depth at the epoch of reionization. Y_p is the fractional primordial abundance of helium. A_S , n_S and α_S are the amplitude, the spectra-index and the running parameter of the primordial power spectrum and we choose the pivot-scale at $k_0 = 0.05$ Mpc. w is the equation of state parameter of the dark energy. N_{eff} is the effective number of the radiative components. b_0 and b_1 are the model parameters for the galaxy biasing parameter. The fiducial values of our choice are

$$\mathbf{p}_{\text{fid}} = \{2.205, 0.1199, 0.6817, f_\nu, 0.089, 0.2477, 0.9603, 2.196, 0, -1, 3.046, 1.0, 0.8\} . \quad (4.3)$$

Our analysis estimates the parameter constraints for the fiducial models with the different values of the lightest neutrino mass $m_{\nu,\text{min}}$. For instance, the fiducial values of $f_\nu \equiv \Omega_\nu/\Omega_m$ are, for the normal (inverted) mass hierarchy scenarios, 0.0012(0.0016), 0.00073(0.0012), 0.00062(0.0010) respectively for $m_{\nu,\text{min}}$ values of 0.05 eV, 0.01 eV and 10^{-4} eV (this last example value 10^{-4} eV can be interpreted as the illustration for the massless minimal neutrino mass). Throughout this paper, we assume a spatially flat Universe and the Hubble parameter is adjusted to keep our Universe flat when we vary the other cosmological parameters.

We first outline the Fisher matrix for the transverse modes, representing the correlations on the projected celestial surface, in terms of the angular power spectrum C_ℓ fully including the auto- and cross-correlations between different observables: the CMB temperature anisotropies, E -mode polarization, CMB lensing potential (T , E , ψ), the galaxy distributions (g_i) and the galaxy weak lensing shear (γ_i). We then briefly review the Fisher matrix for the three-dimensional galaxy power spectrum $P_g(\mathbf{k})$.

4.1 The Fisher matrix for the angular power spectrum

The Fisher matrix for the angular power spectrum is given by [70, 72].

$$F_{\alpha\beta} = \sum_{\ell_{\text{min}}}^{\ell_{\text{max}}} \frac{f_{\text{sky}}(2\ell + 1)}{2} \text{Tr} \left[\frac{\partial \mathbf{C}_\ell}{\partial p_\alpha} \mathbf{C}_\ell^{-1} \frac{\partial \mathbf{C}_\ell}{\partial p_\beta} \mathbf{C}_\ell^{-1} \right] , \quad (4.4)$$

where f_{sky} is the sky coverage of given survey and \mathbf{C}_ℓ represents the covariance matrix for the angular power spectra.

For the angular power spectrum, we consider the CMB and the photometric redshift survey observables ($T, E, \psi, \{g\}, \{\gamma\}$). We take into account the tomographic survey, and $\{g\} = \{g_1, \dots, g_{N_g^{\text{ph}}}\}$ and $\{\gamma\} = \{\gamma_1, \dots, \gamma_{N_\gamma^{\text{ph}}}\}$ represent the spectra from the tomographic redshift bins; N_g^{ph} and N_γ^{ph} are the number of the photometric redshift bins for the galaxy clustering and the galaxy weak lensing observables, respectively.

To take account of the different sky coverage for the CMB and the photometric redshift surveys, we define the total Fisher matrix for the angular power spectrum as

[73];

$$F_{\alpha\beta}^{2D} = f_{\text{sky}}^{\text{LSS}} \sum_{\ell=2}^{\ell_{\text{max}}^{\text{LSS}}} \mathcal{F}_{\ell,\alpha\beta}^{\text{cross}} + (f_{\text{sky}}^{\text{CMB}} - f_{\text{sky}}^{\text{LSS}}) \sum_{\ell=2}^{\ell_{\text{max}}^{\text{LSS}}} \mathcal{F}_{\ell,\alpha\beta}^{\text{CMB}} + f_{\text{sky}}^{\text{CMB}} \sum_{\ell_{\text{max}}^{\text{LSS}}+1}^{\ell_{\text{max}}^{\text{CMB}}} \mathcal{F}_{\ell,\alpha\beta}^{\text{CMB}}, \quad (4.5)$$

with

$$\mathcal{F}_{\ell,\alpha\beta}^{\text{cross}} \equiv \frac{(2\ell+1)}{2} \text{Tr} \left[\frac{\partial \mathbf{C}_{\ell}^{\text{cross}}}{\partial p_{\alpha}} (\mathbf{C}_{\ell}^{\text{cross}})^{-1} \frac{\partial \mathbf{C}_{\ell}^{\text{cross}}}{\partial p_{\beta}} (\mathbf{C}_{\ell}^{\text{cross}})^{-1} \right], \quad (4.6)$$

$$\mathcal{F}_{\ell,\alpha\beta}^{\text{CMB}} \equiv \frac{(2\ell+1)}{2} \text{Tr} \left[\frac{\partial \mathbf{C}_{\ell}^{\text{CMB}}}{\partial p_{\alpha}} (\mathbf{C}_{\ell}^{\text{CMB}})^{-1} \frac{\partial \mathbf{C}_{\ell}^{\text{CMB}}}{\partial p_{\beta}} (\mathbf{C}_{\ell}^{\text{CMB}})^{-1} \right], \quad (4.7)$$

where

$$\mathbf{C}_{\ell}^{\text{cross}} = \begin{pmatrix} C_{\ell}^{TT} + N_{\ell}^T & C_{\ell}^{TE} & C_{\ell}^{T\psi} & C_{\ell}^{T\{\gamma\}} & C_{\ell}^{T\{g\}} \\ C_{\ell}^{TE} & C_{\ell}^{EE} + N_{\ell}^E & 0 & 0 & 0 \\ C_{\ell}^{T\psi} & 0 & C_{\ell}^{\psi\psi} + N_{\ell}^{\psi} & C_{\ell}^{\psi\{\gamma\}} & C_{\ell}^{\psi\{g\}} \\ C_{\ell}^{T\{\gamma\}} & 0 & C_{\ell}^{\psi\{\gamma\}} & C_{\ell}^{\{\gamma\}\{\gamma\}} + N_{\ell}^{\{\gamma\}} & C_{\ell}^{\{\gamma\}\{g\}} \\ C_{\ell}^{T\{g\}} & 0 & C_{\ell}^{\psi\{g\}} & C_{\ell}^{\{\gamma\}\{g\}} & C_{\ell}^{\{g\}\{g\}} + N_{\ell}^{\{g\}} \end{pmatrix}, \quad (4.8)$$

and

$$\mathbf{C}_{\ell}^{\text{CMB}} = \begin{pmatrix} C_{\ell}^{TT} + N_{\ell}^T & C_{\ell}^{TE} & C_{\ell}^{T\psi} \\ C_{\ell}^{TE} & C_{\ell}^{EE} + N_{\ell}^E & \\ C_{\ell}^{T\psi} & 0 & C_{\ell}^{\psi\psi} + N_{\ell}^{\psi} \end{pmatrix}. \quad (4.9)$$

Here the different super-scripts ‘‘CMB’’ and ‘‘LSS’’ represent the variables for the CMB and the photometric redshift surveys, respectively. The label ‘‘cross’’ represents the overlap region between the CMB and the photometric redshift surveys and we assume that the photometric redshift survey fully overlaps with the CMB survey. The covariance matrix \mathbf{C}_{ℓ} and \mathbf{C}_{ℓ} include both signal C_{ℓ}^{XY} and noise

We assume that the cross-correlation between CMB E -mode polarization and the other observables except T should be small because most of E -mode polarization is generated through the Thomson-scattering at the last scattering surface and not produced in the late time Universe ⁵.

For the CMB noise spectra, we simply consider the dominant detector noise represented by the photon shot noise for a single channel [76, 77]

$$N_{\ell,\nu}^{T,E} = (\theta_{\text{FWHM}} \Delta_{\nu}^{T,E})^2 \exp [(\ell(\ell+1)\theta_{\text{FWHM}}^2/8 \ln 2)], \quad (4.10)$$

where θ_{FWHM} is the beam size or the spatial resolution of the beam and Δ_{ν}^X represents the sensitivity of each channel to the temperature Δ_{ν}^T or polarization $\Delta_{\nu}^P = \Delta_{\nu}^E = \Delta_{\nu}^B$,

⁵During the epoch of reionization, some E -mode polarization can be produced and it can correlate with the CMB lensing potential or the objects at the high redshifts [74, 75].

Experiment	f_{sky}	ν [GHz]	θ_{FWHM} [arcmin]	Δ_{ν}^{T} [$\mu\text{K}/\text{pixel}$]	Δ_{ν}^{P} [$\mu\text{K}/\text{pixel}$]
Planck	0.65	100	9.5'	6.8	10.9
		143	7.1'	6.0	11.4
		217	5.0'	13.1	26.7

Table 1. The specifications for the CMB experiment. f_{sky} denotes the fractional sky coverage, ν is the channel frequency, θ_{FWHM} is the beam width and Δ_T (Δ_P) represents the sensitivity of each channel to the temperature (polarization).

Survey	f_{sky}	\bar{n}_{g} [arcmin $^{-2}$]	z_{m}	$\bar{\sigma}_{\gamma}$
DES	0.1	10	0.8	0.3
HSC	0.05	30	1.0	0.3
LSST	0.5	50	1.2	0.3

Table 2. The specifications for the photometric redshift surveys. f_{sky} denotes the fractional sky coverage, \bar{n}_{g} is the surface number density of sample galaxies, z_{m} is the mean redshift of the survey and $\bar{\sigma}_{\gamma}$ denotes the error of shear measurements.

and these values are summarized in Table 1. The corresponding noise power spectrum for a multi-channel experiment is obtained by adding the contribution from all the channels $N_{\ell} = [\sum_{\nu} N_{\ell,\nu}^{-1}]^{-1}$. The noise of the CMB lensing potential N_{ℓ}^{ψ} is estimated as the statistical error of the lensing reconstruction based on the optimal quadratic estimator [71].

The observed shear power spectrum is contaminated by the shear variance per galaxy $\bar{\sigma}_{\gamma}^2$ due to the uncertainties in the intrinsic shape of the source galaxies

$$N_{\ell}^{\gamma i} = \frac{\bar{\sigma}_{\gamma}^2}{\bar{n}_{\text{g},i}} \delta_{ij} . \quad (4.11)$$

Analogously, the noise for the galaxy angular power spectrum is

$$N_{\ell}^{\text{g}i} = \frac{\delta_{ij}}{\bar{n}_{\text{g},i}} , \quad (4.12)$$

where $\bar{n}_{\text{g},i}$ is the number density of sample galaxies per steradian in the i -th tomographic redshift bin and we assume the noise is uncorrelated among different tomographic bins. Throughout this paper, we divide the photometric redshift bins in such a way that the number density of sample galaxies of each redshift bin should be same, $\bar{n}_{\text{g},i} = \bar{n}_{\text{g}}/N^{\text{ph}}$. Table 2 shows the specifications for the photometric redshift surveys used in our analysis.

i	z_c	\bar{n}_g^{3D} [$10^{-3}h^3\text{Mpc}^{-3}$]	V_s/f_{sky} [$h^{-3}\text{Gpc}^{-3}$]	k_{nl} [$h^{-1}\text{Mpc}$]
1	0.26	33.0	10.6	0.12
2	0.61	34.7	11.8	0.15
3	0.77	35.2	13.2	0.16
4	0.92	35.5	14.7	0.18
5	1.06	35.6	16.7	0.20
6	1.20	35.6	18.4	0.21
7	1.35	35.3	22.7	0.23
8	1.53	34.7	30.3	0.25
9	1.77	33.4	44.9	0.29
10	2.45	27.6	182	0.40

Table 3. The survey parameters for the Euclid spectroscopic galaxy redshift survey in our analysis. i denotes the values in the i -th redshift slice, z_c is the central redshift in each redshift bin, V_s and \bar{n}_g^{3D} are the comoving survey volume and number density of sampled galaxies, and $k_{\text{nl}} = \pi/(2R)$ is the wave-number corresponding to the the non-linear scales with the criteria of $\sigma_R(z) = 0.5$. We here adopt the fractional sky coverage $f_{\text{sky}} = 0.2$.

4.2 The Fisher matrix for the three-dimensional galaxy power spectrum

Each redshift slice of the spectroscopic redshift survey provides an independent information and the correlations between different redshift slices should be negligible. The Fisher matrix for the galaxy power spectrum $P_g(\mathbf{k})$ from the spectroscopic redshift survey then reads [72, 78–81];

$$F_{\alpha\beta}^{3D} = \sum_i^{N^{\text{sp}}} \frac{V_{s,i}}{8\pi^2} \int_{-1}^1 d\mu \int_{k_{\text{min}}}^{k_{\text{max}}} k^2 dk \frac{\partial P_g(k, \mu, z_{c,i})}{\partial p_\alpha} \frac{\partial P_g(k, \mu, z_{c,i})}{\partial p_\beta} \left[\frac{P_g(k, \mu, z_{c,i})}{P_g(k, \mu, z_{c,i}) + 1/\bar{n}_{g,i}^{3D}} \right]^2, \quad (4.13)$$

where N^{ph} is the number of the redshift slices, z_c is the central redshift of the redshift bin, \bar{n}_g^{3D} and V_s are respectively the mean comoving galaxy number density and the comoving volume of the galaxy survey, and the sub-script i denotes the value in the i -th redshift slice. We summarize these values in each redshift slice in Table 3, and these estimations are carried out as follows.

The mean comoving number density of the sample galaxies is determined as

$$\bar{n}_{g,i}^{3D} = \int_{M_{\text{min}}}^{\infty} dM n_h(M, z_{c,i}) \langle N \rangle_M, \quad (4.14)$$

where the functions n_h is the halo mass function for a given mass M and a redshift z . We use the mass function $n_h(M, z)$ given by Warren et. al. [82]. $\langle N \rangle_M$ is the halo-occupation distribution describing how many galaxies the halo with th mass M hosts, and we here simply assume $\langle N \rangle_M = 1$. The parameter M_{min} is the minimum halo mass

Survey	Observables	f_{sky}	ℓ_{min} or k_{min}	ℓ_{max} or k_{max}	redshift bin
Planck	CMB (T, E, ψ)	0.65	2	3000	—
LSST	photo- z (g, γ)	0.5	2	500	5
Euclid	spec- z ($g^{3\text{D}}$)	0.2	$10^{-4} h/\text{Mpc}$	k_{nl}	10

Table 4. The reference survey model in our analysis.

hosting the observed galaxies, which corresponds to the observational limits of each survey. We here simply set $M_{\text{min}} = 10^{11.0} M_{\odot}/h$ for all redshifts.

The comoving survey volume is approximately defined as

$$V_{s,i} \simeq 4\pi f_{\text{sky}} r(z_{c,i})^2 \frac{dr}{dz} \Delta z_i \quad (4.15)$$

where Δz_i denotes the width of i -th redshift slice.

For the range of the k -integration, we set the maximum wave-number k_{max} to avoid using the nonlinear k modes. We used the criteria for the linear scale $k < k_{\text{max}}$ by demanding the amplitude of the smoothed density field $\sigma_R(z) < 0.5$, so that $k_{\text{max}} = \pi/(2R)$ for $\sigma_R(z) = 0.5$. The variance of the smoothed density field here is given by

$$\sigma_R^2(z) = \frac{1}{2\pi^2} \int k^2 P_m(k) W(kR)^2 \frac{D(z)^2}{D(0)^2} dk, \quad (4.16)$$

The function $W(kR)$ is the top-hat window function, R is the smoothing scale, and D_0 is the growth factor at the present time. For the minimum wave-number, we simply choose $k_{\text{min}} = 10^{-4} h/\text{Mpc}$ for all the redshift slices.

In combining the Fisher matrix of $P_g(\mathbf{k})$ including both transverse and longitudinal mode information and that of C_l including only the transverse mode information, to avoid the complications in the full covariance matrix, we make a simplified assumption that their transverse modes are fully correlated and take account of the common transverse modes only once [83–85]. Accordingly, in our combining the spectroscopic galaxy redshift survey with the photometric galaxy survey for an overlapping sky area, we remove the section around $\mu = 0$ in integrating the Fisher matrix over μ not to over-count the transverse modes in estimating the parameter uncertainties⁶. This hence would give us a conservative estimation for the total information by combining these measurements and the actual cosmological parameter uncertainties would be smaller due to the smaller cross correlations among the common transverse modes in $P_g(\mathbf{k})$ and C_ℓ .

We put the constraints on the cosmological parameters by combining the upcoming data from three kinds of the survey projects. The first is the CMB experiment by the Planck satellite which provides the temperature anisotropies (T), the E -mode polarization (E) and the weak lensing of the CMB (ψ ; the lensing potential). The second

⁶More rigorous treatment to cross-correlate the three-dimensional and two-dimensional data will be presented in our separate forthcoming paper.

is the photometric redshift survey by the LSST which provides the information of the galaxy clustering (g) and the galaxy weak lensing (γ ; the lensing shear). The third is the spectroscopic redshift survey by the Euclid which provides the 3-dimensional galaxy power spectrum (g^{3D}). We use these projects as our fiducial survey models and the survey parameters are summarized in Table 4.

5 Results

We here present the results of our forecasts for the cosmological parameters illustrating the breaking of the parameter degeneracies by combining the various observables. Figures 1 and 2 show the projected 1- σ confidence limit (CL) contours on each parameter plane for, respectively, the normal and inverted mass hierarchy scenarios with the lightest neutrino mass $m_{\nu,\min} = 0.01$ eV. These panels compare the constraints for four cases ; 1) ‘‘CMB + γ ’’ combines the CMB and galaxy weak lensing observables. 2) ‘‘CMB + g’’ combines the CMB and galaxy clustering observables. 3) ‘‘CMB + g + γ ’’ combines the CMB, galaxy weak lensing and galaxy clustering observables. 4) ‘‘CMB + g + γ + g^{3D} ’’ combines the CMB, galaxy clustering, galaxy weak lensing observables plus the 3-dimensional galaxy power spectrum. We adopt the Planck for the CMB, the LSST for the galaxy weak lensing and the photometric galaxy redshift survey, and the Euclid for the spectroscopic galaxy redshift survey. We take into account all the auto- and cross-correlations among these observables. Table 5 summarizes the projected 1- σ error of each parameter for the normal and inverted mass hierarchy scenarios for a few representative lightest neutrino masses $m_{\nu,\min} = 10^{-4}$ and 0.01 and 0.05 eV ⁷.

A big advantage of adding the redshift survey to the CMB observables is the breaking of the angular diameter distance degeneracies [86]. For the photometric redshift surveys, for instance, the galaxy weak lensing information is helpful in breaking the $\sum m_\nu$ - w degeneracy [12]. (This $\sum m_\nu$ - w degeneracy arises indirectly from the degeneracy between w - Ω_Λ and that between $\sum m_\nu$ - Ω_Λ . w and Ω_Λ are degenerate in affecting the late time Hubble expansion rate, while $\sum m_\nu$ and Ω_Λ (or equivalently Ω_m) are degenerate affecting the matter power spectrum suppression scale.) The lensing weight $W_{\ell,i}(r)$ (Eq. (3.6)) is sensitive to the dark energy parameters, Ω_Λ and w , because the distance-redshift relation $r = \int dz/H(z)$ is affected by the dark energy properties. Hence adding the galaxy weak lensing information helps to constrain the dark energy parameters and it consequently improves the neutrino mass constraints (even though the light neutrinos of our interest would not directly affect the the late time Hubble expansion rate). In particular, the tomographic survey gives an additional handle on the distance-redshift relation due to the different redshift dependence of $W_{\ell,i}(r)$ for each redshift bin, which further helps in breaking the w - Ω_Λ degeneracy.

While the neutrino masses are already tightly constrained from the angular power spectra including the CMB and photometric redshift survey data with all the cross correlations taken into account, we found adding the three-dimensional galaxy power spectrum $P_g(\mathbf{k})$ still helps in further improving the neutrino mass determination by as

⁷ $m_{\nu,\min} = 10^{-4}$ eV essentially represents the massless lightest neutrino case as demonstrated in Figure 4.

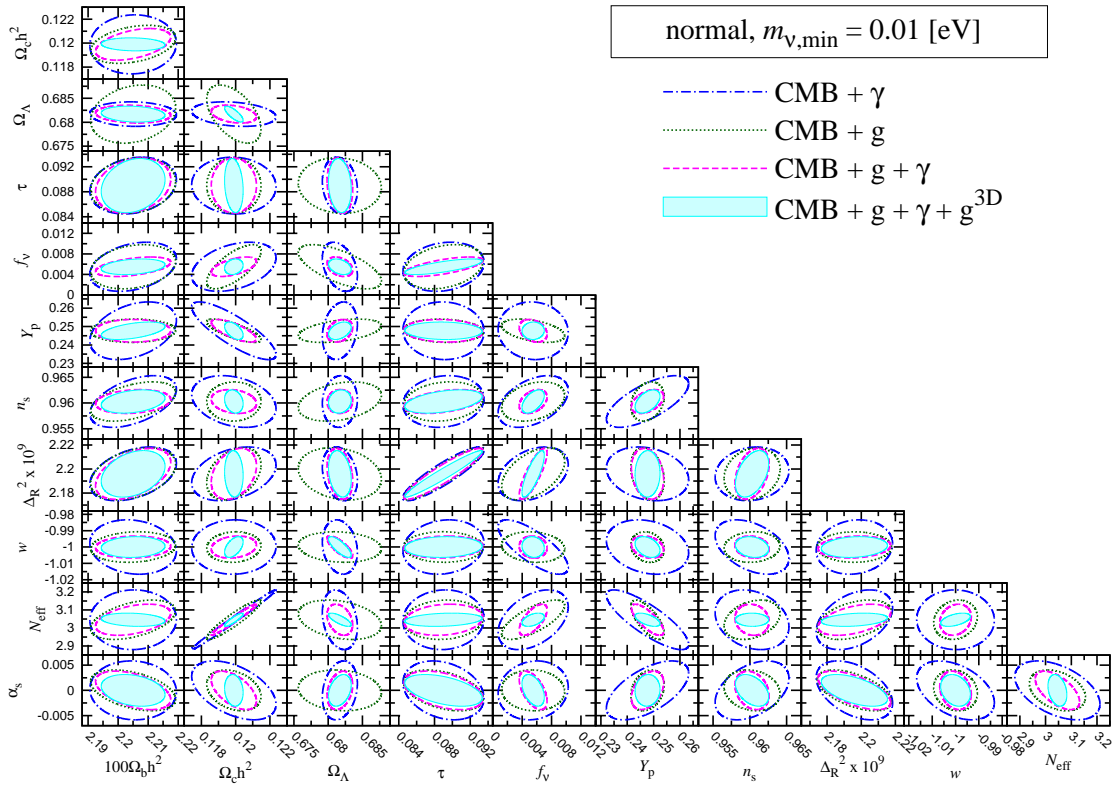


Figure 1. The projected $1\text{-}\sigma$ (68%) CL areas on each parameter plane for the normal mass hierarchy scenario with the lightest neutrino mass $m_{\nu,\min} = 0.01$ eV. We compare the four combinations of the observables from the Planck (T, E, ψ), LSST (g, γ) and Euclid (g^{3D}); 1) (blue) CMB and galaxy weak lensing (T, E, ψ, γ), 2) (green) CMB and galaxy clustering (T, E, ψ, g), 3) (magenta) CMB, galaxy clustering and weak lensing (T, E, ψ, g, γ), and 4) (cyan) CMB, galaxy clustering, weak lensing and 3-dimensional galaxy power spectrum ($T, E, \psi, g, \gamma, g^{3D}$).

much as 20-40 % depending on the neutrino mass structure as shown in Table 5. This improvement stems from the reduction of the galaxy bias uncertainty by cross correlating the different observables [11, 73, 88]. From the transverse mode information in the 2-dimensional angular correlations, the galaxy bias can be inferred from the ratios of the galaxy power spectrum (dependent on the bias squared), the lensing shear power (independent of the bias) and their cross correlation (linearly dependent on the bias), because they have the different dependence on the bias. Adding the 3-dimensional galaxy power spectrum $P_g(\mathbf{k})$ with the redshift space distortion to the 2-dimensional angular power spectra C_l further reduces, in addition to adding more modes, the uncertainties in the galaxy bias from the comparison of the clustering along the transverse and the line of sight directions because the bias affects only the density growth not the velocity growth along the line of sight. Combining these different probes on the galaxy bias would lead to a better handle on the determination of the galaxy bias and

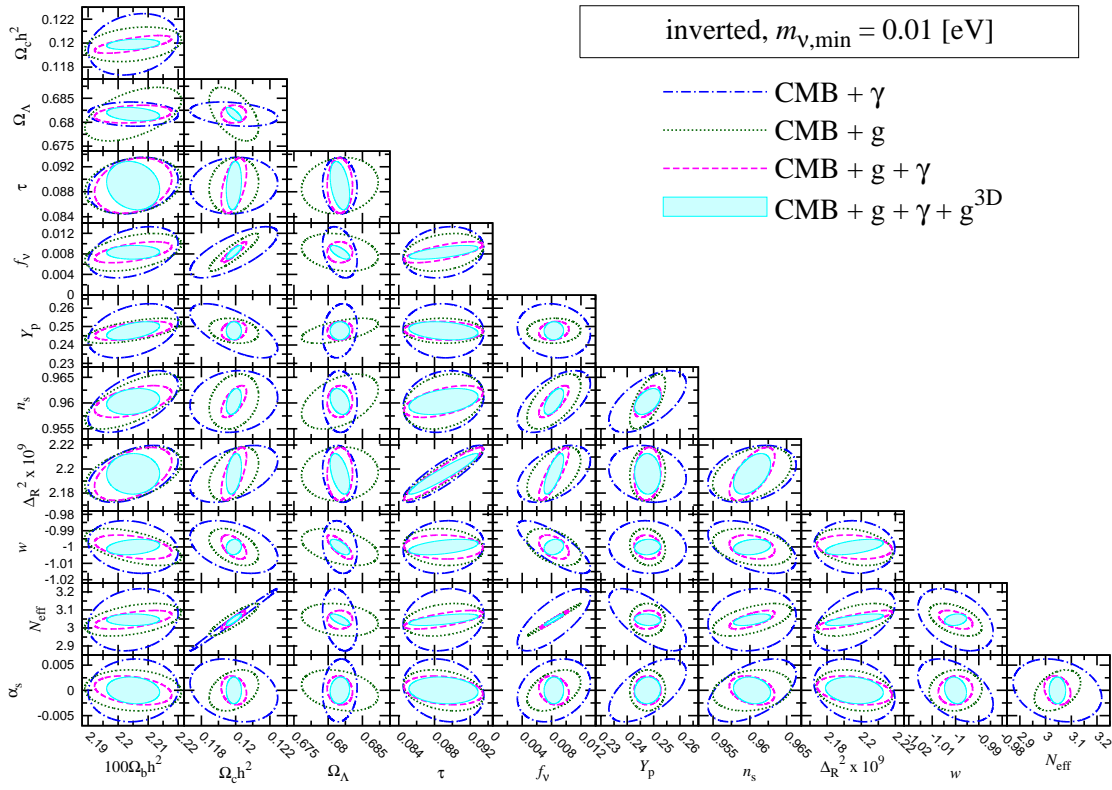


Figure 2. Same as Figure 1, but for the inverted mass hierarchy scenario with the same value of the lightest neutrino mass.

consequently a better measurement of the other cosmological parameters which suffer from the degeneracies with the galaxy bias. For instance, the resultant improvement in estimating the growth rate results in the better estimation of the equation of state parameter w [85], and hence the degeneracy between $\sum m_\nu$ and w can be broken to improve the neutrino mass constraint.

In Figure 3, we show the projected $1\text{-}\sigma$ CL contours on the f_ν - b_0 and f_ν - b_1 planes, i.e. the degeneracies between the effects of non-relativistic neutrinos and the galaxy biasing parameters. Although the galaxy biasing parameters have strong degeneracies with f_ν , the combination of the multiple observables with the different dependence on the bias parameters indeed helps breaking the degeneracies with the galaxy bias. The observables such as the CMB and the galaxy weak lensing (γ) which are not directly affected by the galaxy bias are also useful for the improvement on the bias estimations because they induce the cross correlations with the observables directly affected by the bias.

Figure 4 shows the predicted uncertainties in $\sum m_\nu$ as a function of the lightest neutrino mass $m_{\nu,\min}$. We should note that the mass splittings are fixed to be consistent with the oscillation data whose values are given by Eq. (1.1). Our future cosmolog-

Normal hierarchy: $m_{\nu,\min} = m_1 < m_2 \ll m_3$

Observables	$100\Omega_b h^2$	$\Omega_c h^2$	Ω_Λ	τ	f_ν	Y_p	n_S	$A_S \times 10^9$	w	N_{eff}	α	b_0	b_1	$\sum m_\nu$
$m_{\nu,\min} = 0.05$ eV														
CMB (T, E, ψ)	0.023	0.00410	0.0893	0.0045	0.0123	0.0170	0.0107	0.025	0.3436	0.265	0.0080	—	—	0.202
γ	1.247	0.04021	0.0042	—	0.0282	—	0.0770	0.617	0.0410	0.766	0.0293	—	—	0.707
g	0.024	0.00581	0.0129	—	0.0219	—	0.0334	0.477	0.0123	0.626	0.0296	0.0757	0.0338	0.348
CMB + γ	0.015	0.00278	0.0024	0.0045	0.0050	0.0155	0.0060	0.023	0.0181	0.187	0.0061	—	—	0.091
CMB + g	0.016	0.00148	0.0054	0.0044	0.0035	0.0071	0.0052	0.021	0.0094	0.104	0.0040	0.0153	0.0086	0.061
CMB + g + γ	0.013	0.00116	0.0017	0.0043	0.0019	0.0068	0.0031	0.021	0.0068	0.078	0.0031	0.0032	0.0035	0.035
CMB + g + γ + g^{3D} (spec- z)	0.013	0.00052	0.0014	0.0043	0.0014	0.0064	0.0030	0.019	0.0056	0.035	0.0026	0.0029	0.0031	0.024
$m_{\nu,\min} = 0.01$ eV														
CMB (T, E, ψ)	0.023	0.00408	0.0907	0.0045	0.0136	0.0170	0.0107	0.025	0.3570	0.265	0.0079	—	—	0.199
γ	1.397	0.04402	0.0054	—	0.0188	—	0.0713	0.479	0.0427	0.722	0.0268	—	—	0.417
g	0.168	0.00778	0.0135	—	0.0146	—	0.0226	0.270	0.0135	0.449	0.0165	0.0664	0.0204	0.229
CMB + γ	0.014	0.00246	0.0025	0.0045	0.0047	0.0156	0.0050	0.022	0.0166	0.165	0.0058	—	—	0.073
CMB + g	0.014	0.00158	0.0060	0.0044	0.0042	0.0063	0.0038	0.021	0.0093	0.109	0.0040	0.0135	0.0112	0.064
CMB + g + γ	0.012	0.00132	0.0018	0.0043	0.0018	0.0061	0.0023	0.021	0.0067	0.086	0.0038	0.0032	0.0039	0.030
CMB + g + γ + g^{3D} (spec- z)	0.010	0.00054	0.0016	0.0043	0.0015	0.0047	0.0022	0.019	0.0063	0.036	0.0031	0.0026	0.0031	0.022
$m_{\nu,\min} = 10^{-4}$ eV														
CMB (T, E, ψ)	0.023	0.00407	0.0896	0.0046	0.0126	0.0169	0.0106	0.025	0.3474	0.264	0.0079	—	—	0.181
γ	0.844	0.02851	0.0048	—	0.0140	—	0.0588	0.401	0.0430	0.692	0.0253	—	—	0.277
g	0.172	0.00434	0.0181	—	0.0098	—	0.0333	0.260	0.0132	0.488	0.0126	0.1061	0.0322	0.149
CMB + γ	0.015	0.00275	0.0031	0.0045	0.0049	0.0151	0.0058	0.023	0.0220	0.188	0.0058	—	—	0.074
CMB + g	0.016	0.00107	0.0051	0.0044	0.0029	0.0059	0.0054	0.021	0.0085	0.086	0.0041	0.0153	0.0066	0.042
CMB + g + γ	0.014	0.00090	0.0016	0.0043	0.0017	0.0052	0.0031	0.021	0.0065	0.059	0.0029	0.0031	0.0032	0.026
CMB + g + γ + g^{3D} (spec- z)	0.010	0.00048	0.0013	0.0042	0.0014	0.0051	0.0028	0.017	0.0060	0.029	0.0027	0.0030	0.0029	0.020

Inverted hierarchy: $m_{\nu,\min} = m_3 \ll m_1 < m_2$

Observables	$100\Omega_b h^2$	$\Omega_c h^2$	Ω_Λ	τ	f_ν	Y_p	n_S	$A_S \times 10^9$	w	N_{eff}	α	b_0	b_1	$\sum m_\nu$
$m_{\nu,\min} = 0.05$ eV														
CMB (T, E, ψ)	0.023	0.00413	0.0896	0.0045	0.01188	0.0170	0.0107	0.025	0.3416	0.267	0.0079	—	—	0.200
γ	1.193	0.03283	0.0049	—	0.02943	—	0.0492	0.347	0.0433	0.643	0.0269	—	—	0.715
g	0.025	0.00484	0.0164	—	0.00116	—	0.0201	0.236	0.0566	0.378	0.0129	0.0420	0.0434	0.042
CMB + γ	0.015	0.00346	0.0025	0.0044	0.00383	0.0131	0.0067	0.023	0.0168	0.213	0.0063	—	—	0.080
CMB + g	0.016	0.00174	0.0110	0.0036	0.00064	0.0077	0.0052	0.017	0.0390	0.124	0.0039	0.0240	0.0091	0.020
CMB + g + γ	0.012	0.00147	0.0023	0.0033	0.00064	0.0070	0.0023	0.013	0.0091	0.089	0.0032	0.0046	0.0047	0.018
CMB + g + γ + g^{3D} (spec- z)	0.012	0.00066	0.0019	0.0028	0.00061	0.0058	0.0022	0.012	0.0079	0.042	0.0029	0.0039	0.0033	0.014
$m_{\nu,\min} = 0.01$ eV														
CMB (T, E, ψ)	0.023	0.00407	0.0921	0.0046	0.0126	0.0170	0.0107	0.025	0.3574	0.263	0.0079	—	—	0.193
γ	1.323	0.03858	0.0049	—	0.0230	—	0.0810	0.543	0.0388	0.568	0.0243	—	—	0.529
g	0.081	0.00494	0.0131	—	0.0152	—	0.0246	0.421	0.0395	0.364	0.0216	0.0454	0.0406	0.236
CMB + γ	0.015	0.00255	0.0025	0.0045	0.0049	0.0146	0.0060	0.023	0.0161	0.172	0.0062	—	—	0.081
CMB + g	0.016	0.00144	0.0055	0.0044	0.0036	0.0067	0.0053	0.022	0.0112	0.090	0.0040	0.0142	0.0071	0.057
CMB + g + γ	0.012	0.00073	0.0018	0.0044	0.0020	0.0050	0.0030	0.022	0.0073	0.051	0.0028	0.0031	0.0032	0.032
CMB + g + γ + g^{3D} (spec- z)	0.010	0.00044	0.0014	0.0038	0.0013	0.0049	0.0025	0.016	0.0047	0.032	0.0026	0.0029	0.0029	0.020
$m_{\nu,\min} = 10^{-4}$ eV														
CMB (T, E, ψ)	0.023	0.00409	0.0919	0.0045	0.0128	0.0170	0.0107	0.025	0.3575	0.265	0.0079	—	—	0.194
γ	1.220	0.04075	0.0058	—	0.0138	—	0.0673	0.416	0.0420	0.670	0.0298	—	—	0.367
g	0.267	0.01182	0.0157	—	0.0064	—	0.0406	0.159	0.0157	0.036	0.0098	0.0854	0.0435	0.143
CMB + γ	0.013	0.00233	0.0026	0.0045	0.0030	0.0151	0.0045	0.021	0.0145	0.152	0.0059	—	—	0.051
CMB + g	0.015	0.00071	0.0050	0.0043	0.0020	0.0077	0.0045	0.019	0.0093	0.016	0.0036	0.0145	0.0104	0.031
CMB + g + γ	0.013	0.00037	0.0017	0.0037	0.0011	0.0059	0.0024	0.016	0.0066	0.014	0.0033	0.0035	0.0043	0.017
CMB + g + γ + g^{3D} (spec- z)	0.012	0.00035	0.0011	0.0036	0.0010	0.0058	0.0023	0.016	0.0053	0.013	0.0033	0.0030	0.0036	0.015

Table 5. The projected 1- σ (68%) CL error of each parameter for the the normal (Top) and inverted (Bottom) mass hierarchy scenarios with the lightest neutrino masses of $m_{\nu,\min} = 0.05, 0.01$ and 10^{-4} eV. The first three rows respectively list the constraints from only the CMB(T, E, ψ), the galaxy weak lensing (γ) and the galaxy clustering (g). The next four rows represent the results with different combinations of the observables. The last row combines all the CMB, the galaxy weak lensing, the galaxy clustering observables and the 3-dimensional galaxy power spectrum (CMB + g + γ + g^{3D} (spec- z)).

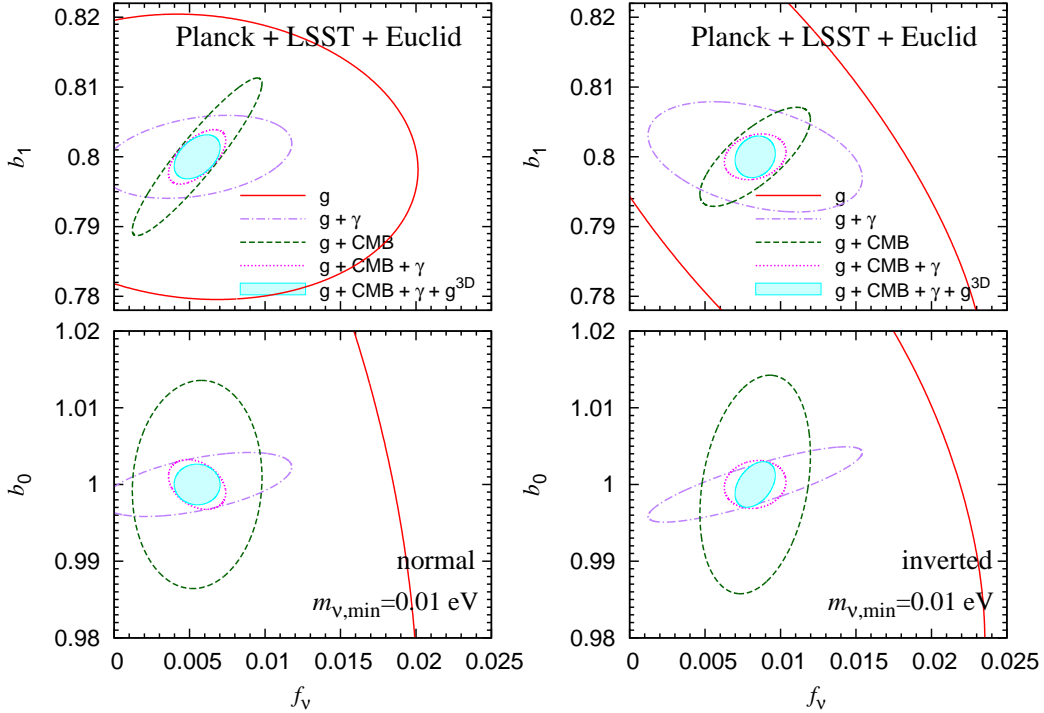


Figure 3. The degeneracies with the galaxy bias parameters (b_0, b_1). The contours show the the projected $1\text{-}\sigma$ CL areas on the f_ν - b_0 (Bottom) and f_ν - b_1 (Top) planes for the normal (Left) and inverted (Right) mass hierarchy scenarios with the lightest neutrino mass $m_{\nu, \min} = 0.01$ eV. Each line and filled area represent the constraints with the different combinations of the observables from Planck (CMB), LSST (g and γ) and Euclid (g^{3D}); 1) the galaxy clustering alone (red), 2) the galaxy clustering and the galaxy weak lensing (purple), 3) the galaxy clustering and CMB (green), 4) the galaxy clustering, the galaxy weak lensing and the CMB (magenta), 5) the galaxy clustering, the galaxy lensing, CMB and the three-dimensional galaxy power spectrum (cyan).

ical observables we have been discussing can probe the sum of neutrino masses and still would not be sensitive enough to differentiate each neutrino mass. Even though the neutrino effects on the cosmological observables become bigger and hence a bigger total neutrino mass results in the smaller parameter uncertainties, the distinction between the normal and inverted mass patterns becomes harder for a sufficiently large $m_{\nu, \min}$ leading to the quasi-degenerate mass spectra $m_1 \sim m_2 \sim m_3$. On the other hand, the smaller neutrino mass leads to the smaller effects on the matter power and consequently results in the bigger uncertainties in the parameter estimations. We fortunately find that the neutrino mass splitting values provided by the current oscillation data give a big enough sum of the neutrino masses, even with the lightest neutrino species being massless, for the forthcoming cosmological experiments to be capable of distinguishing between the normal and inverted mass patterns with the predicted one-sigma uncertainties taken into account.

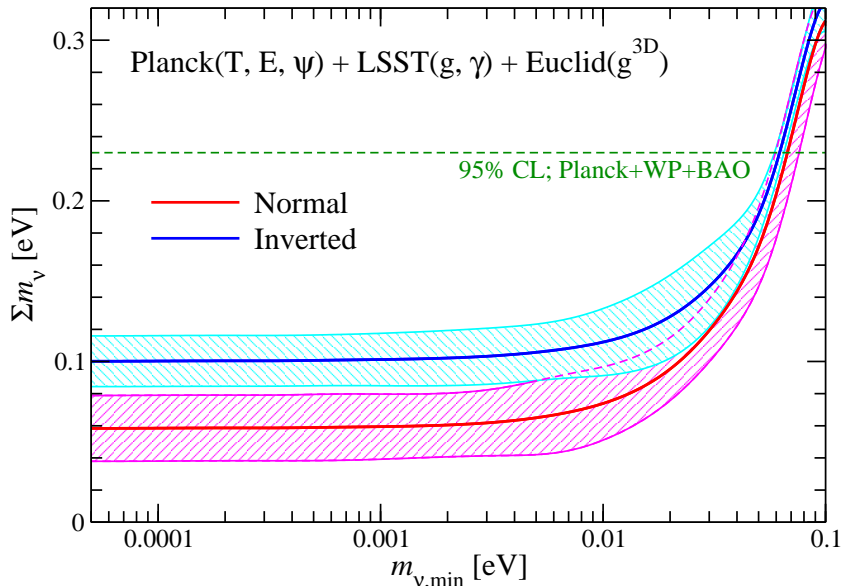


Figure 4. The projected $1\text{-}\sigma$ error for the total neutrino mass $\sum m_\nu$ as a function of the lightest neutrino mass $m_{\nu,\min}$ for the normal (red) and inverted (blue) mass hierarchy scenarios. The thick solid curves representing the fiducial $\sum m_\nu$ for a given $m_{\nu,\min}$ are obtained using the mass difference values from the neutrino oscillation data (given by Eq. (1.1)). The filled curves represent the $1\text{-}\sigma$ CL regions estimated by combining all the observables (T , E , ψ , g , γ and g^{3D}), and we assume Planck for the CMB, LSST for the galaxy clustering and the galaxy weak lensing observables, and Euclid for the 3-dimensional galaxy power spectrum.

Our analysis can claim that the measurement of $\sum m_\nu$ from the combination of the future cosmological observations can distinguish between the normal and inverted mass hierarchy scenarios for $m_{\nu,\min} \lesssim 0.005$ eV without the overlap in the error bars. The relative difference between the normal and inverted mass spectrum becomes smaller for $m_{\nu,\min} \gtrsim 0.005$ eV with the overlapped error bars in $\sum m_\nu$, and it would become harder to cosmologically distinguish the two where the mass spectra would eventually be rather interpreted, for a sufficiently large $m_{\nu,\min}$, as the quasi-degenerate mass spectrum $m_{\nu_1} \sim m_{\nu_2} \sim m_{\nu_3}$ within the predicted uncertainties. The constraint on the total neutrino mass saturates for $m_{\nu,\min} \lesssim 0.001$ eV where the contribution of the lightest neutrino mass to the total mass becomes negligible.

We can also obtain further information on the neutrino properties by combining the cosmological data with those from other neutrino experiments such as the neutrino double beta decay whose observables have the different dependence on the minimal neutrino mass or neutrino mass structure [3]. For a common value of $m_{\nu,\min}$, $\sum m_\nu$ is bigger for the inverted mass spectrum than for the normal mass spectrum. The neutrino effects on the large-scale structures or the matter power spectrum hence generally appear more clearly for the inverted mass hierarchy, which offers tighter constraints, in particular, on the density parameter of cold dark matter $\Omega_c h^2$, the fraction of the massive neutrinos f_ν , and the effective number of the radiative components N_{eff} . We

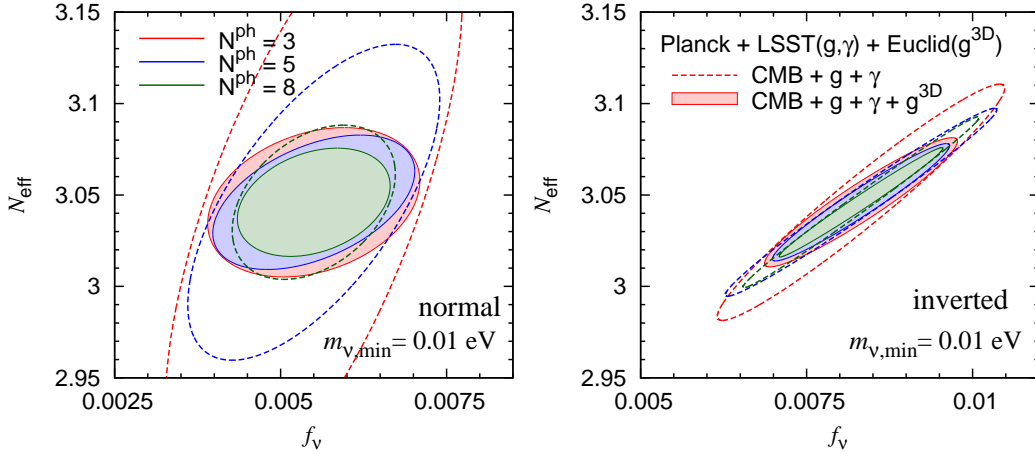


Figure 5. The comparison of the constraints with different number of redshift bins for the photometric redshift survey. The contours show the projected $1\text{-}\sigma$ (68%) CL areas for the normal (Left) and inverted (Right) mass hierarchies with the lightest neutrino mass $m_{\nu,\min} = 0.01$ eV. For the illustrating purpose, we assume the same number of redshift bins for the galaxy clustering and the galaxy weak lensing surveys, i.e. $N^{\text{ph}} = N_{\text{g}}^{\text{ph}} = N_{\gamma}^{\text{ph}}$. The dashed-curves represent the constraints from the CMB, the galaxy clustering and the galaxy weak lensing observables, whereas the filled-areas represent the constraints from the CMB, the galaxy clustering, the galaxy weak lensing observables and the 3-dimensional galaxy power spectrum from the spectroscopic redshift survey. The different colors show the different number of the photometric redshift bins; $N^{\text{ph}} = 3$ (red), 5 (blue) and 8 (green), respectively. The number of the redshift bins of the spectroscopic galaxy redshift survey is fixed to be $N^{\text{sp}} = 10$ for all cases.

also note that the inverted (as well as the normal) mass hierarchy scenario can be excluded or inconsistent with the cosmological observations if we do not observe the effects of the massive neutrinos for $\sum m_{\nu}$ below the values given by the lower boundary of the (blue (red) shaded) $1\text{-}\sigma$ region in Figure 4.

6 Discussion and conclusion

Although we so far presented our results with the concrete fiducial experiment setups, we now study how the neutrino parameter estimations would change if we change the survey specifications. For an illustration purpose, we here compare the different photometric redshift survey specifications, firstly by changing the redshift bin numbers of the fiducial LSST survey and secondly by considering, instead of the future LSST survey, the on-going photometric redshift surveys: DES and HSC.

While our fiducial survey model assumed the number of redshift bins for the photometric redshift survey to be $N^{\text{ph}} = 5$, the number of redshift bins is one of the key components in the survey strategy affecting the constraints on the cosmological parameters. We hence here briefly discuss how the parameter estimation can be affected

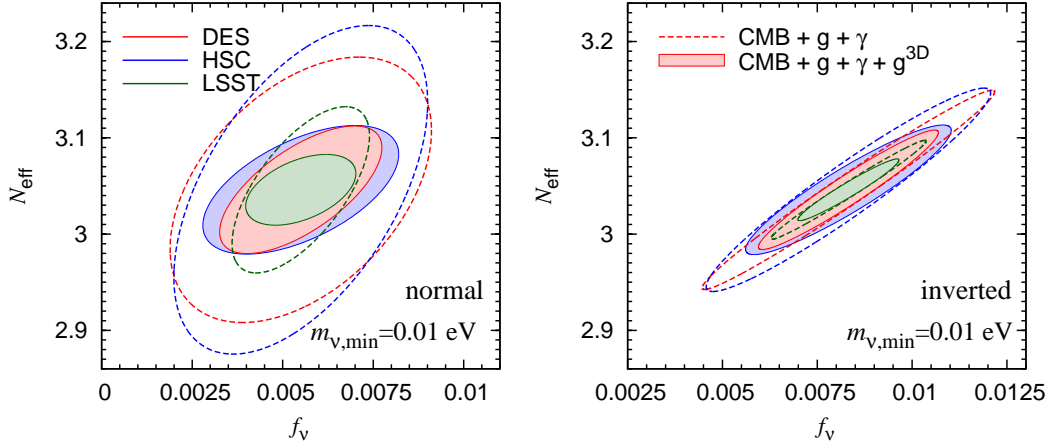


Figure 6. The comparison among the different photometric redshift surveys. The contours show the projected $1\text{-}\sigma$ (68%) CL areas for the normal (Left) and inverted (Right) mass hierarchies, and we here use the fiducial model with the lightest neutrino mass of $m_{\nu,\min} = 0.01$ eV. The dashed-curves represent the constraints from the combination of the CMB, the galaxy clustering and the galaxy weak lensing observables, whereas the filled-areas represent the constraints from the CMB, the galaxy clustering, the galaxy weak lensing and the 3-dimensional galaxy power spectrum. The different colors represent the different photometric redshift surveys; DES (red), HSC (blue) and LSST (green), respectively, and we assume Planck for CMB and Euclid for the spectroscopic galaxy redshift survey for all cases.

by varying the number of the photometric redshift bins N^{ph} . We assume the same number of the redshift bins for the galaxy clustering and the galaxy weak lensing observables, $N^{\text{ph}} = N_g^{\text{ph}} = N_\gamma^{\text{ph}}$, for simplicity. Figure 5 shows the results on the f_ν - N_{eff} plane for the different number of the photometric redshift bins, $N^{\text{ph}} = 3, 5$ and 8. We compare two cases for each number of N^{ph} ; one is the combination of the Planck and the LSST surveys, and the other is the combination of the Planck, the LSST and the Euclid surveys. The number of redshift bins for the spectroscopic survey is fixed to be $N^{\text{sp}} = 10$ and the lightest neutrino mass $m_{\nu,\min} = 0.01$ eV was used for all cases.

The normal mass hierarchy scenario benefits more from the increase in the number of redshift bins, whereas the results for the inverted hierarchy are saturated around $N^{\text{ph}} = 5\text{-}8$. This is partly because the cosmological observables are sensitive to the total neutrino mass and the normal mass spectrum leads to the smaller sum of the neutrino masses than the inverted one for a common value of the lightest neutrino mass.

The next comparison we will make here is for the different photometric redshift surveys to see their effects on the the neutrino property estimations. Even though we so far focused on the photometric redshift survey by the LSST as an ultimate survey in the next decade, the forecasts from the on-going experiments would be of great interest and we here investigate how the neutrino properties can be constrained by the DES and HSC surveys. The survey parameters for the DES and HSC are shown in Table 2.

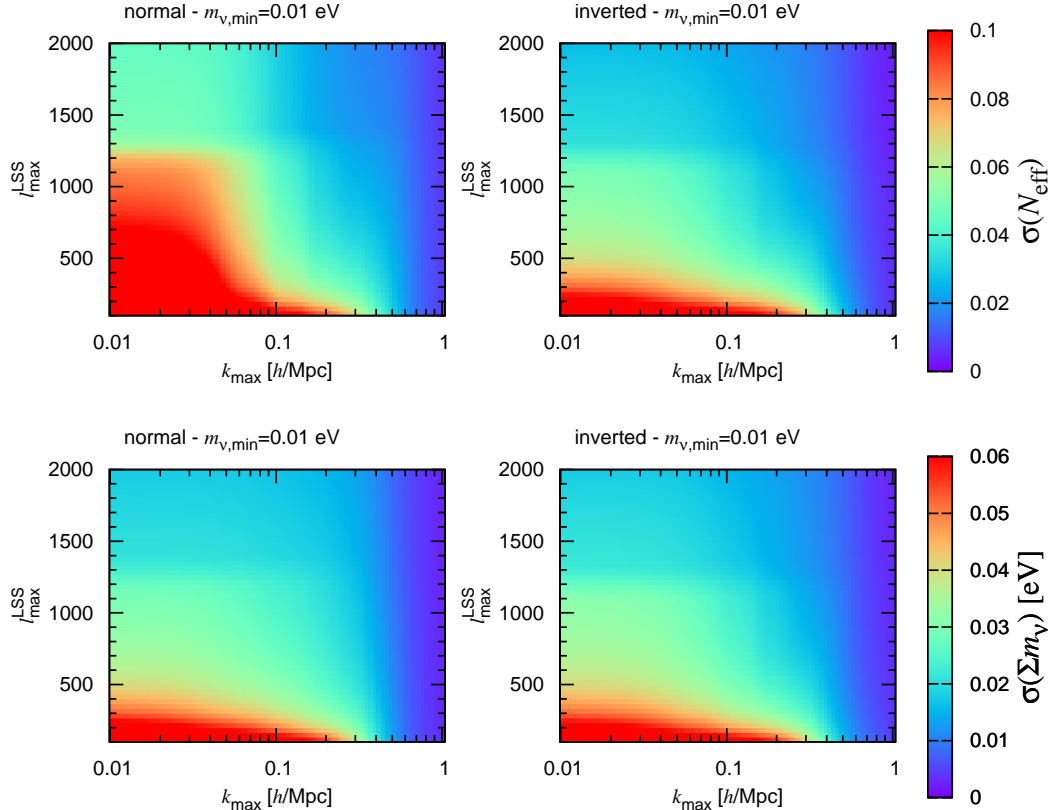


Figure 7. The dependence of the projected 1σ error of the neutrino parameter on the maximum wave-number k_{\max} for the spectroscopic galaxy redshift survey, and the maximum multipole moment ℓ_{\max}^{LSS} for the photometric redshift surveys. The color bars represent the projected $1\text{-}\sigma$ constraint on the effective number $\sigma(N_{\text{eff}})$ (Top) and the total neutrino mass $\sigma(\sum m_\nu)$ (Bottom) for the normal (Left) and inverted (Left) mass hierarchies with the lightest neutrino mass of $m_{\nu,\min} = 0.01$ eV. We put the constraint on each parameter from the combination of the Planck, LSST and Euclid surveys (CMB + g + γ + $g^{3\text{D}}$) and the maximum multipole moment for the CMB observables is fixed to be $\ell_{\max} = 3000$.

Figure 6 shows the comparison on the f_ν - N_{eff} plane for both the normal and inverted mass hierarchies with $m_{\nu,\min} = 0.01$ eV. Analogously to Figure 5, we show two kinds of constraints for the combination of the observables; one is for the combination of the Planck and the LSST surveys, and the other is for the combination of the Planck and the LSST surveys plus the spectroscopic redshift survey by the Euclid. The constraints on the neutrino parameters from the DES and HSC surveys are comparable, whereas those from the LSST survey are much tighter. The differences of constraints between the DES and HSC surveys come from the depth of the observing redshift range and the survey area, and the DES survey is slightly superior to the HSC survey for the constraints on the neutrino properties in this case. For the total neutrino mass, the DES and HSC surveys can potentially achieve $\sigma(\sum m_\nu) \sim 0.03$ eV in our example, even though the LSST can reduce the neutrino mass uncertainties by as much as 50% for

the normal hierarchy and even more for the inverted hierarchy by a factor 2.

Before concluding our discussions, let us lastly point out that we conservatively restricted our analysis to the linear regime with the corresponding choice for ℓ_{\max} and k_{\max} . The inclusion of more modes covering the bigger ℓ_{\max} and k_{\max} would be of particular interest for the neutrinos sensitive to the small scale structures. We conservatively chose the relatively small values for ℓ_{\max} and k_{\max} to avoid taking account of the non-Gaussian error estimation at the non-linear scales, even though we could have chosen larger values for higher redshift bins as discussed in Sec. 4.

For an illustration purpose, we try extending our linear analysis to the smaller scales to see how the constraints are influenced under the assumption of the Gaussian error estimation, though the results may over/under predict the constraints due to the lack of the non-Gaussian error estimation [89, 90]. The estimation of the matter power spectrum at the non-linear scales may also affect the constraints of the neutrino properties and we refer the readers to, for instance, Ref. [55, 91] for the more appropriate treatments including the non-linearities in existence of the light neutrino species. We show the k_{\max} and ℓ_{\max} dependence of the uncertainties in the effective number of neutrinos and the total neutrino mass parameters in Figure 7 which assumes the data from the CMB, galaxy clustering, galaxy weak lensing observables and the 3-dimensional galaxy power spectrum with the Planck, LSST and Euclid. We use the same value ℓ_{\max}^{LSS} for the maximum multipole of the galaxy clustering and the galaxy weak lensing observables for comparison purposes, and the maximum multipole of the CMB observables is fixed to be $\ell_{\max}^{\text{CMB}} = 3000$. The fiducial model is the normal or inverted mass hierarchy scenario with the lightest neutrino mass $m_{\nu, \min} = 0.01$ eV.

The constraint on N_{eff} mainly comes from the large-scales via the shift in the turn-over scale of the matter power spectrum, but the information from the small-scales helps to break the degeneracy with other cosmological parameters. Compared with the inverted mass hierarchy, the normal mass hierarchy leads to the smaller total neutrino mass, and consequently the degeneracies with other parameters are stronger. For the constraints on $\sum m_{\nu}$, the difference between the normal and inverted mass hierarchies is not as large as that on N_{eff} , even though the saturation scale of k_{\max} for the normal mass hierarchy is slightly larger than the inverted mass hierarchy. We note that the uncertainty for $\sum m_{\nu}$ saturates at the order of $\sigma(\Omega_{\text{m}} h^2)$ because of the degeneracy between $\sum m_{\nu}$ and $\Omega_{\text{m}} h^2$.

We studied how much the constraints on the neutrino properties are improved by combining the various observables from the next-generation cosmological surveys with the cross-correlations taken into account among those observables. We in particular studied, for the fiducial neutrino models, the normal and inverted mass hierarchy scenarios consisting of three neutrino species where the neutrino mass splittings are fixed to those values obtained by the neutrino oscillation measurements and the only free neutrino mass parameter hence is the minimal neutrino mass. We also studied how the cosmological parameter errors are affected by the different choices of a minimal neutrino mass value. For the reference cosmological surveys, the Planck CMB, LSST photometric redshift survey and Euclid spectroscopic redshift survey are assumed,

where the forecasted uncertainties in the neutrinos were found to be in the range $\sigma(\sum m_\nu) \sim 0.015\text{-}0.025$ eV and $\sigma(N_{\text{eff}}) \sim 0.03$. We also estimated the projected cosmological errors assuming the on-going photometric galaxy surveys such as the DES and HSC to compare with the LSST, and we found the neutrino mass uncertainties increase by as much as a factor 2.

The merits of adding the spectroscopic redshift survey information with the redshift space distortion to the two dimensional observables including the CMB lensing and galaxy weak lensing survey were emphasized to break the degeneracies among the parameters, such as those between the neutrino and dark energy parameters. A better handle on the galaxy bias was argued to be responsible for the improvement in the parameter estimation, and, in particular, the improvement for the neutrino mass estimation amounts to 20 – 40% depending on the neutrino mass hierarchical structure. The power of the future cosmological observables to distinguish between the normal and inverted neutrino mass hierarchy scenarios was also quantified. We found the measurement of the total neutrino mass can well distinguish between the normal and inverted mass hierarchy scenarios for $m_{\nu,\text{min}} \lesssim 0.005$ eV. We restricted our analysis to the linear regime and extending our analysis to a smaller scale in principle can potentially reduce the projected errors. The outcome would however heavily depend on the treatment of non-linearities, and the more proper treatment including for instance the non-Gaussian covariance would be necessary to probe those smaller scales.

Finally, we should note the accuracy of the Fisher matrix analysis for the constraint on neutrino masses. Especially for small neutrino masses, the constraint by the Fisher matrix analysis might not be completely accurate because the assumption of the Gaussian posterior could be no longer valid, e.g., [9, 22, 31, 35]. The potential quantitative differences between the Fisher matrix and the Monte Carlo Markov Chain (MCMC) approaches for constraining the neutrinos from the CMB observation are presented, for instance, in [9, 31], and we leave the the analysis with the MCMC approach and its comparison with that using the Fisher analysis for our future work.

The neutrino properties in combination of other experiments besides the cosmological observables such as the accelerator neutrinos and neutrinoless double beta decay experiments would certainly deserve the further studies as a unique window to the physics beyond the Standard Model.

Acknowledgement

This work was supported in part by the Grant-in-Aid for the Global COE program and for Scientific Research from the JSPS. We thank Kobayashi-Maskawa Institute for the Origin of Particles and the Universe; Nagoya University for providing computing resources in conducting the research reported in this paper, the Aspen Center for Physics and the Kavli Institute for Theoretical Physics China where part of this work was conducted.

References

- [1] B. Pontecorvo, Sov. Phys. JETP **6**, 429 (1957) [Zh. Eksp. Teor. Fiz. **33**, 549 (1957)].
- [2] Z. Maki, M. Nakagawa, S. Sakata and , Prog. Theor. Phys. **28**, 870 (1962).
- [3] K. Nakamura and S. T. Petcov, "Neutrino Masses, Mixing and Oscillations"; in J. Beringer *et al.* [Particle Data Group Collaboration], Phys. Rev. D **86**, 010001 (2012).
- [4] Z. Hou, C. L. Reichardt, K. T. Story, B. Follin, R. Keisler, K. A. Aird, B. A. Benson and L. E. Bleem *et al.*, arXiv:1212.6267 [astro-ph.CO].
- [5] P. A. R. Ade *et al.* [Planck Collaboration], arXiv:1303.5080 [astro-ph.CO].
- [6] W. Hu and S. Dodelson, Ann. Rev. Astron. Astrophys. **40**, 171 (2002) [astro-ph/0110414].
- [7] K. N. Abazajian and S. Dodelson, Phys. Rev. Lett. **91**, 041301 (2003) [astro-ph/0212216].
- [8] J. Lesgourgues, L. Perotto, S. Pastor and M. Piat, Phys. Rev. D **73**, 045021 (2006) [astro-ph/0511735].
- [9] L. Perotto, J. Lesgourgues, S. Hannestad, H. Tu, and Y. Y Y Wong, JCAP **10** (Oct., 2006) 13, [arXiv:astro-ph/0606227].
- [10] G. L. Fogli, E. Lisi, A. Marrone, A. Melchiorri, A. Palazzo, P. Serra, J. Silk and A. Slosar, Phys. Rev. D **75**, 053001 (2007) [hep-ph/0608060].
- [11] M. Takada, E. Komatsu and T. Futamase, Phys. Rev. D **73**, 083520 (2006) [astro-ph/0512374].
- [12] S. Hannestad, H. Tu and Y. Y. Y. Wong, JCAP **0606**, 025 (2006) [astro-ph/0603019].
- [13] U. Seljak, A. Slosar, P. McDonald and , JCAP **0610**, 014 (2006) [astro-ph/0604335].
- [14] F. De Bernardis, P. Serra, A. Cooray, A. Melchiorri and , Phys. Rev. D **78**, 083535 (2008) [arXiv:0809.1095 [astro-ph]].
- [15] V. Acquaviva, A. Hajian, D. N. Spergel and S. Das, Phys. Rev. D **78**, 043514 (2008) [arXiv:0803.2236 [astro-ph]].
- [16] K. Ichiki, M. Takada and T. Takahashi, Phys. Rev. D **79** (2009) 023520 [arXiv:0810.4921 [astro-ph]].
- [17] A. Vikhlinin, A. V. Kravtsov, R. A. Burenin, H. Ebeling, W. R. Forman, A. Hornstrup, C. Jones and S. S. Murray *et al.*, Astrophys. J. **692**, 1060 (2009) [arXiv:0812.2720 [astro-ph]].
- [18] F. De Bernardis, T. D. Kitching, A. Heavens and A. Melchiorri, Phys. Rev. D **80**, 123509 (2009) [arXiv:0907.1917 [astro-ph.CO]].
- [19] A. Mantz, S. W. Allen, D. Rapetti Mon. Not. Roy. Astron. Soc. **406**, 1805 (2010) [arXiv:0911.1788 [astro-ph.CO]].
- [20] M. C. Gonzalez-Garcia, M. Maltoni and J. Salvado, JHEP **1008**, 117 (2010) [arXiv:1006.3795 [hep-ph]].
- [21] T. Namikawa, S. Saito and A. Taruya, JCAP **1012**, 027 (2010) [arXiv:1009.3204

- [astro-ph.CO]].
- [22] S. Galli, M. Martinelli, A. Melchiorri, L. Pagano, B. D. Sherwin, D. N. Spergel, *Phys. Rev. D* **82**, 123504 (2010) [arXiv:astro-ph/1005.3808v1].
- [23] K. N. Abazajian, E. Calabrese, A. Cooray, F. De Bernardis, S. Dodelson, A. Friedland, G. M. Fuller and S. Hannestad *et al.*, *Astropart. Phys.* **35**, 177 (2011) [arXiv:1103.5083 [astro-ph.CO]].
- [24] C. Carbone, L. Verde, Y. Wang and A. Cimatti, *JCAP* **1103**, 030 (2011) [arXiv:1012.2868 [astro-ph.CO]].
- [25] J. Hamann, S. Hannestad and Y. Y. Y. Wong, arXiv:1209.1043 [astro-ph.CO].
- [26] X. Wang, X. -L. Meng, T. -J. Zhang, H. Shan, Y. Gong, C. Tao, X. Chen and Y. F. Huang arXiv:1210.2136 [astro-ph.CO].
- [27] R. A. Burenin, A. A. Vikhlinin arXiv:1202.2889 [astro-ph.CO].
- [28] A. G. Sanchez, C. G. Scoccola, A. J. Ross, W. Percival, M. Manera, F. Montesano, X. Mazzalay and A. J. Cuesta *et al.*, arXiv:1203.6616 [astro-ph.CO].
- [29] S. Joudaki and M. Kaplinghat, *Phys. Rev. D* **86**, 023526 (2012) [arXiv:1106.0299 [astro-ph.CO]].
- [30] C. Carbone, C. Fedeli, L. Moscardini and A. Cimatti, *JCAP* **1203**, 023 (2012) [arXiv:1112.4810 [astro-ph.CO]].
- [31] A. C. Hall and A. Challinor, arXiv:1205.6172 [astro-ph.CO].
- [32] R. A. Vanderveld, W. Hu and , arXiv:1212.3608 [astro-ph.CO].
- [33] M. C. A. Cerbolini, B. Sartoris, J. -Q. Xia, A. Biviano, S. Borgani, M. Viel and , arXiv:1303.4550 [astro-ph.CO].
- [34] E. Giusarma, R. de Putter, S. Ho and O. Mena, arXiv:1306.5544 [astro-ph.CO].
- [35] B. Audren, J. Lesgourgues, S. Bird, M. G. Haehnelt, and M. Viel, *JCAP* **1** (Jan., 2013) 26, arXiv:1210.2194].
- [36] P. A. R. Ade *et al.* [Planck Collaboration], arXiv:1303.5062 [astro-ph.CO].
- [37] D. Hanson *et al.* [SPTpol Collaboration], arXiv:1307.5830 [astro-ph.CO].
- [38] M. D. Niemack, P. A. R. Ade, J. Aguirre, F. Barrientos, J. A. Beall, J. R. Bond, J. Britton and H. M. Cho *et al.*, *Proc. SPIE Int. Soc. Opt. Eng.* **7741**, 77411S (2010) [arXiv:1006.5049 [astro-ph.IM]].
- [39] S. Miyazaki, Y. Komiyama, H. Nakaya, Y. Doi, H. Furusawa, P. Gillingham, Y. Kamata, K. Takeshi, and K. Nariai, *HyperSuprime: project overview*, in *Society of Photo-Optical Instrumentation Engineers (SPIE) Conference Series*, vol. 6269, July, 2006.
- [40] The Dark Energy Survey Collaboration, *The Dark Energy Survey, ArXiv Astrophysics e-prints* (Oct., 2005) [arXiv:astro-ph/0510346].
- [41] LSST Science Collaborations, P. A. Abell, J. Allison, S. F. Anderson, J. R. Andrew, J. R. P. Angel, L. Armus, D. Arnett, S. J. Asztalos, T. S. Axelrod, and et al., *LSST Science Book, Version 2.0, ArXiv e-prints* (Dec., 2009) [arXiv:0912.0201].

- [42] R. Laureijs, J. Amiaux, S. Arduini, J. . Auguères, J. Brinchmann, R. Cole, M. Cropper, C. Dabin, L. Duvet, A. Ealet, and et al., *Euclid Definition Study Report, ArXiv e-prints* (Oct., 2011) [arXiv:1110.3193].
- [43] G. L. Fogli, E. Lisi, A. Marrone, D. Montanino, A. Palazzo, A. M. Rotunno, *Phys. Rev. D* **86**, 013012 (2012) [arXiv:1205.5254 [hep-ph]].
- [44] J. Lesgourgues and S. Pastor, *Phys. Rept.* **429**, 307 (2006) [astro-ph/0603494].
- [45] S. Bashinsky and U. Seljak, *Phys. Rev. D* **69**, 083002 (2004) [astro-ph/0310198].
- [46] S. Dodelson, E. Gates and A. Stebbins, *Astrophys. J.* **467**, 10 (1996) [astro-ph/9509147].
- [47] G. Efstathiou, J. R. Bond, *Mon. Not. Roy. Astron. Soc.* **304**, 75 (1999) [astro-ph/9807103].
- [48] C. Howlett, A. Lewis, A. Hall, A. Challinor and , *JCAP* **1204**, 027 (2012) [arXiv:1201.3654 [astro-ph.CO]].
- [49] K. N. Abazajian, E. Calabrese, A. Cooray, F. De Bernardis, S. Dodelson, A. Friedland, G. M. Fuller and S. Hannestad *et al.*, *Astropart. Phys.* **35**, 177 (2011) [arXiv:1103.5083 [astro-ph.CO]].
- [50] W. Hu and T. Okamoto, *Astrophys. J.* **574**, 566 (2002) [astro-ph/0111606].
- [51] J. R. Bond, G. Efstathiou and J. Silk, *Phys. Rev. Lett.* **45**, 1980 (1980).
- [52] J. Lesgourgues, S. Pastor and L. Perotto, *Phys. Rev. D* **70** (2004) 045016 [hep-ph/0403296].
- [53] D. J. Eisenstein and W. Hu, *Astrophys. J.* **511**, 5 (1997) [astro-ph/9710252].
- [54] W. Hu, D. J. Eisenstein and , *Astrophys. J.* **498**, 497 (1998) [astro-ph/9710216].
- [55] S. Bird, M. Viel and M. G. Haehnelt, *Mon. Not. Roy. Astron. Soc.* **420**, 2551 (2012) [arXiv:1109.4416 [astro-ph.CO]].
- [56] W. Hu, D. J. Eisenstein and M. Tegmark, *Phys. Rev. Lett.* **80**, 5255 (1998) [astro-ph/9712057].
- [57] A. Lewis, A. Challinor, and A. Lasenby, *Astrophys. J* **538** (Aug., 2000) 473–476, [arXiv:astro-ph/9911177].
- [58] R. K. Sachs and A. M. Wolfe, *Astrophys. J* **147** (Jan., 1967) 73–+.
- [59] A. Lewis and A. Challinor, *Phys. Rep.* **429** (June, 2006) 1–65, [arXiv:astro-ph/0601594].
- [60] D. H. Weinberg, R. Davé, N. Katz, and L. Hernquist, *Astrophys. J* **601** (Jan., 2004) 1–21, [arXiv:astro-ph/0212356].
- [61] I. Smail, R. S. Ellis, and M. J. Fitchett, *Mon. Not. R. Astron. Soc.* **270** (Sept., 1994) 245, [arXiv:astro-ph/9402048].
- [62] A. Amara and A. Réfrégier, *Mon. Not. R. Astron. Soc.* **381** (Nov., 2007) 1018–1026, [arXiv:astro-ph/0610127].
- [63] Z. Ma, W. Hu, and D. Huterer, *Astrophys. J* **636** (Jan., 2006) 21–29, [arXiv:astro-ph/0506614].

- [64] N. Kaiser, *Mon. Not. R. Astron. Soc.* **227** (July, 1987) 1–21.
- [65] C. Alcock and B. Paczynski, *Nature* **281** (Oct., 1979) 358.
- [66] T. Matsubara and Y. Suto, *Astrophys. J Lett.* **470** (Oct., 1996) L1, [[arXiv:astro-ph/9604142](#)].
- [67] W. E. Ballinger, J. A. Peacock, and A. F. Heavens, *Mon. Not. R. Astron. Soc.* **282** (Oct., 1996) 877, [[arXiv:astro-ph/9605017](#)].
- [68] H.-J. Seo and D. J. Eisenstein, *Astrophys. J* **598** (Dec., 2003) 720–740, [[arXiv:astro-ph/0307460](#)].
- [69] D. Hanson, A. Challinor and A. Lewis, *Gen. Rel. Grav.* **42**, 2197 (2010) [[arXiv:0911.0612 \[astro-ph.CO\]](#)].
- [70] W. Hu and B. Jain, *Phys. Rev. D* **70**, 043009 (2004) [[astro-ph/0312395](#)].
- [71] T. Okamoto and W. Hu, *Phys. Rev. D* **67** (Apr., 2003) 083002+, [[arXiv:astro-ph/0301031](#)].
- [72] M. Tegmark, A. N. Taylor, and A. F. Heavens, *Astrophys. J* **480** (May, 1997) 22+, [[arXiv:astro-ph/9603021](#)].
- [73] Y. Takeuchi, K. Ichiki, and T. Matsubara, *Phys. Rev. D* **85** (Feb., 2012) 043518, [[arXiv:1111.6835](#)].
- [74] A. Lewis, A. Challinor, and D. Hanson, *JCAP* **3** (Mar., 2011) 18, [[arXiv:1101.2234](#)].
- [75] C. Dvorkin and K. M. Smith, *Phys. Rev. D* **79** (Feb., 2009) 043003, [[arXiv:0812.1566](#)].
- [76] L. Knox, *Phys. Rev. D* **52**, 4307 (1995) [[astro-ph/9504054](#)].
- [77] J. R. Bond, G. Efstathiou and M. Tegmark, *Mon. Not. Roy. Astron. Soc.* **291**, L33 (1997) [[astro-ph/9702100](#)].
- [78] N. Kaiser, *Mon. Not. Roy. Astron. Soc.* **227**, 1 (1987).
- [79] H. A. Feldman, N. Kaiser and J. A. Peacock, *Astrophys. J.* **426**, 23 (1994) [[astro-ph/9304022](#)].
- [80] M. Tegmark, *Phys. Rev. Lett.* **79**, 3806 (1997) [[astro-ph/9706198](#)].
- [81] H. -J. Seo and D. J. Eisenstein, *Astrophys. J.* **598**, 720 (2003) [[astro-ph/0307460](#)].
- [82] M. S. Warren, K. Abazajian, D. E. Holz, and L. Teodoro, *Astrophys. J* **646** (Aug., 2006) 881–885, [[arXiv:astro-ph/0506395](#)].
- [83] A. J. Nishizawa, M. Oguri and M. Takada, [arXiv:1302.6015 \[astro-ph.CO\]](#).
- [84] Y. -C. Cai and G. Bernstein, *Mon. Not. Roy. Astron. Soc.* **422**, 1045 (2012) [[arXiv:1112.4478 \[astro-ph.CO\]](#)].
- [85] E. Gaztanaga, M. Eriksen, M. Crocce, F. Castander, P. Fosalba, P. Marti, R. Miquel and A. Cabre, [arXiv:1109.4852 \[astro-ph.CO\]](#).
- [86] D. J. Eisenstein, W. Hu and M. Tegmark, *Astrophys. J.* **518**, 2 (1999) [[astro-ph/9807130](#)].
- [87] A. Challinor and A. Lewis, *Phys. Rev. D* **71**, 103010 (2005) [[astro-ph/0502425](#)].
- [88] U. -L. Pen, *Mon. Not. Roy. Astron. Soc.* **350**, 1445 (2004) [[astro-ph/0402008](#)].

- [89] M. Sato and T. Nishimichi, *Phys. Rev. D* **87** (June, 2013) 123538, [arXiv:1301.3588].
- [90] I. Kayo, M. Takada, and B. Jain, *Mon. Not. R. Astron. Soc.* **429** (Feb., 2013) 344–371, [arXiv:1207.6322].
- [91] S. Hannestad, T. Haugbølle and C. Schultz, *JCAP* **1202**, 045 (2012) [arXiv:1110.1257 [astro-ph.CO]].